A hydrophobic core in the coiled-coil domain is essential for NRC resistosome function

Hung-Yu Wang[1,2,3], Enoch Lok Him Yuen[4], Kim-Teng Lee[1,2,3], Foong-Jing Goh[1,2,3], Tolga O. Bozkurt[4], Chih-Hang Wu[1,2,5]*

[1] Institute of Plant and Microbial Biology, Academia Sinica, Taipei 115201, Taiwan
[2] Molecular and Biological Agricultural Sciences Program, Taiwan International Graduate Program, National Chung-Hsing University and Academia Sinica, Taipei 115201, Taiwan
[3] Graduate Institute of Biotechnology, National Chung-Hsing University, Taichung 402202, Taiwan
[4] Department of Life Sciences, Imperial College London, London SW7 2AZ, UK
[5] Biotechnology Center, National Chung-Hsing University, Taichung 402202, Taiwan

*Correspondence to wuchh@gate.sinica.edu.tw

Abstract

The nucleotide-binding leucine-rich repeat protein (NLR) required for cell death (NRC) family represents a group of helper NLRs that are required by sensor NLRs to execute hypersensitive cell death during pathogen infection. NRCs contain an N-terminal coiled-coil (CC) domain essential for their function, yet our knowledge of how this domain contributes to NRC function remains limited. Here, we identified a novel hydrophobic feature within the CC domain that contributes to NRC-mediated immunity. We screened for conserved hydrophobic residues among NRCs and identified seven required for NRC4-mediated cell death. Structural analysis revealed that four of these residues form a hydrophobic core in the CC domain. This hydrophobic core is important for NRC4 subcellular localization, oligomerization, and phospholipid association, but not for NRC4 focal accumulation at the extrahaustorial membrane during *Phytophthora infestans* infection. Sequence analysis and functional assays revealed this core is highly conserved in NRCs and some singleton NLRs but has degenerated in NRC-dependent sensor NLRs. Our study identifies a novel hydrophobic feature in the CC domain of NRCs and reveals its contribution to NLR-mediated immunity.

Keywords: plant immunity, nucleotide-binding leucine-rich repeat protein (NLR), NLR-required for cell death (NRC), resistosome, coiled-coil domain

38 **Introduction**

39

40 Plants, as immobile organisms, have evolved sophisticated immune receptor systems to detect and
41 respond to pathogen attacks (Jones & Dangl, 2006; Ngou *et al*, 2021; Jones *et al*, 2024). Among these
42 defense mechanisms, nucleotide-binding leucine-rich repeat proteins (NLRs) serve as intracellular
43 immune sensors that recognize pathogen effectors and initiate hypersensitive cell death to restrict
44 pathogen proliferation (Jones & Dangl, 2006; Duxbury *et al*, 2021).

45

46 NLRs consist of three canonical domains: the N-terminal domain, the NB-ARC domain, and the LRR
47 domain (Duxbury *et al*, 2021). Based on their N-terminal domains, NLRs are classified into three
48 main types: CC-NLRs (CNLs) containing a coiled-coil domain, TIR-NLRs (TNLs) with a
49 Toll/interleukin-1 receptor domain, and CC_R-NLRs (RNLs) possessing a Resistance to Powdery
50 Mildew 8 (RPW8)-like domain (Duxbury *et al*, 2021). Different N-terminal domains mediate distinct
51 downstream events leading to NLR-triggered immunity. In TNLs, the TIR domain functions as an
52 NADase enzyme, producing phosphoribosyl adenosine monophosphate/diphosphate (pRib-AMP/ADP)
53 or cyclic ADPR (cADPR) isomers that initiate immune signaling (Ma *et al*, 2020; Martin *et al*, 2020;
54 Huang *et al*, 2022; Jia *et al*, 2022; Yu *et al*, 2024). Mutations in the enzymatic residues essential for
55 NADase activity disrupt immune signaling and impair TNL function (Wan *et al*, 2019; Ma *et al*,
56 2020). Recent studies on CNLs and RNLs have demonstrated that their CC domains play crucial roles
57 in membrane association, with these proteins likely functioning as calcium-permeable channels upon
58 activation to trigger cell death (Wang *et al*, 2019a; Bi *et al*, 2021; Jacob *et al*, 2021). Mutations in
59 positively charged residues involved in membrane association or negatively charged residues critical
60 for ion channel activity disrupt cell death mediated by some CNLs and RNLs (Bi *et al*, 2021; Jacob *et*
61 *al*, 2021; Saile *et al*, 2021; Wang *et al*, 2023).

62

63 While some NLRs like ZAR1 act as functional singletons that both recognize effectors and initiate
64 immune responses, others have undergone functional specialization, evolving into sensor NLRs that
65 detect effectors and helper NLRs that activate immune responses (Wu *et al*, 2017, 2018; Adachi *et al*,
66 2019b; Contreras *et al*, 2023a; Shepherd *et al*, 2023). The NLR-required for cell death (NRC) family
67 represents a group of helper NLRs that form a complex network with phylogenetically related sensor
68 NLRs, particularly expanded in asterid plants (Wu *et al*, 2017; Goh *et al*, 2024; Sakai *et al*, 2024). In
69 solanaceous plants, NRC2, NRC3, and NRC4 are the three major NRCs that function with various
70 sensor NLRs, forming a complex immune network against a broad range of pathogens (Wu *et al*,
71 2017). Some sensor NLRs rely on a single NRC for immunity signaling, while others utilize multiple
72 NRCs, highlighting the genetic redundancy within the NRC network. For example, the sensor NLR
73 *Rpi-blb2*, which detects the RXLR effector AVRblb2 delivered by *Phytophthora infestans*, signals

through NRC4, whereas another sensor NLR, Rx, which detects the coat protein of potato virus X, signals through NRC2/3/4 in *Nicotiana benthamiana* (Wu *et al*, 2017).

Recent cell biology and cryo-EM studies have revealed that NRCs transition from cytosolic dimer complexes in their resting state to membrane-associated hexameric resistosome complexes upon activation (Madhuprakash *et al*, 2024; Liu *et al*, 2024; Selvaraj *et al*, 2024; Ma *et al*, 2024). In the resting state, NbNRC2 protomers form homodimers with unique dimerization interfaces in the cytosol that likely prevent unwanted cross-activation between different NRC helpers (Selvaraj *et al*, 2024). Additionally, studies on tomato NRC2 (SlNRC2), an ortholog of NbNRC2, revealed that, in addition to homodimers, SlNRC2 assembles into filamentous structures that likely serve to regulate its activity negatively (Ma *et al*, 2024). Upon activation by sensor NLRs, the NbNRC homodimers dissociate and oligomerize into hexameric resistosome complexes on the plasma membrane (Wang *et al*, 2023; Liu *et al*, 2024). Notably, NbNRC4 resistosomes function as ion-permeable channels that enable calcium influx, ultimately inducing hypersensitive cell death (Liu *et al*, 2024). This role of hexameric NRC resistosomes aligns with findings from the pentameric AtZAR1 and TmSr35 resistosomes, which also form ion channels on the plasma membrane to trigger cell death (Wang *et al*, 2019a; Liu *et al*, 2024; Förderer *et al*, 2022).

During *P. infestans* infection, the pathogen forms haustoria that penetrate plant cells to deliver effectors and obtain nutrients (Wang *et al*, 2017; Bozkurt & Kamoun, 2020). These haustoria are surrounded by a specialized, newly-synthesized plant membrane called the extrahaustorial membrane (EHM) (Bozkurt & Kamoun, 2020; Yuen *et al*, 2023). To successfully colonize the host, *P. infestans* secretes a range of RXLR effectors across the EHM to facilitate the infection (Bozkurt *et al*, 2011; Wang *et al*, 2019b; King *et al*, 2024). Among these, the RXLR effector AVRblb2 accumulates at the EHM and targets the secretion of papain-like cysteine protease C14, thereby suppressing immune responses (Bozkurt *et al*, 2011, 201). Interestingly, NRC4 focally accumulates at the EHM during infection, even in the absence of its cognate sensor NLR Rpi-blb2 (Duggan *et al*, 2021). Upon activation, NRC4 forms puncta on both the EHM and the plasma membrane. Recent research has highlighted the importance of interactions between NRC4 and phosphatidylinositol phosphates, such as PI4P, which are also present on the EHM (Rausche *et al*, 2021; Wang *et al*, 2023). However, the extent to which NRC4-lipid interactions influence its localization at the EHM and the plasma membrane remains to be determined.

As a member of the CNL family, NRC4 contains four α helices in its CC domain (Liu *et al*, 2024). The first α helix harbors a conserved MADA motif, which is shared by NRC helper proteins and ZAR1 but not by NRC-dependent sensor NLRs (Adachi *et al*, 2019a). Mutations in the hydrophobic residues of the MADA motif disrupt NRC and ZAR1-mediated cell death, highlighting the

importance of hydrophobicity within this region for NRC function (Adachi *et al*, 2019a). However, the contributions of the other α helices in the CC domain to NRC4 function remain unknown.

In this study, we identified a novel hydrophobic core formed by the α2–α4 helices of the NRC4 CC domain which plays a critical role in NRC4-mediated immunity. Mutations in this hydrophobic core impaired NRC4 subcellular localization, resistosome formation, and NRC4-phospholipid association without affecting its focal accumulation at the EHM during *P. infestans* infection. Further investigation revealed that the corresponding residues in this hydrophobic core are highly conserved in NRC helper NLRs and some singleton NLRs like ZAR1 and Rpi-vnt1.1 but have diverged in NRC-dependent sensor NLRs. Moreover, while this hydrophobic feature is functionally important in ZAR1, Rpi-vnt1.1, and NRCs, it appears to have degenerated in sensor NLRs. Our findings reveal a previously uncharacterized hydrophobic element at the center of the CC domain that is essential for NRC4 subcellular localization, resistosome formation, and phospholipid binding, and is conserved across NRC helper NLRs and some singleton NLRs, providing new insights into the structural basis of NLR-mediated immunity in plants.

Results

Mutations of conserved hydrophobic residues in the CC domain compromise the cell death activity of NRC4

The N-terminal CC domain in CNLs comprises four alpha helices (α1~α4) crucial for resistosome function (Wang *et al*, 2019a; Liu *et al*, 2024). In NRC4 and most other NRCs, the α1 helix contains a MADA motif essential for mediating cell death (Adachi *et al*, 2019a). However, how α2-4 helices in the CC domain contribute to the NRC function is not clear. To dissect the function of these alpha helices in NRC4-mediated cell death, we perform a full-length protein sequence alignment of NRC4 with NRC2, NRC3, and AtZAR1. We identified 19 conserved hydrophobic residues across the three alpha helices of NRCs and AtZAR1 (Fig. S1). To determine which residues are essential for NRC4 function, we mutated those hydrophobic residues (L/A/I/V/F) to the hydrophilic residue glutamic acid (E). We then tested their cell death activities by co-expression with Rpi-blb2 and AVRblb2 in the *nrc2/3/4*_KO *N. benthamiana* and quantified the cell death by using auto-fluorescence-based imaging (Fig. 1A). Among the 19 NRC4 variants, we found that single mutations at L34, F44, A72, I114, V118, L121, and L128 fully impaired NRC4-mediated cell death (Fig. 1B). Protein accumulation levels of these NRC4 mutants with compromised cell death showed no significant difference compared to the wild-type (Fig. S2A, B), indicating that the reduced NRC4-mediated cell death was not due to changes in protein stability. In total, we identified mutations in 2 residues in α2, 1 residue in α3, and 4 residues in α4 of the CC domain that compromised NRC4-mediated cell death.

To test whether these 7 mutations also compromise the cell death induced by an autoactive NRC4 mutation, we introduced them individually into the NRC4^{D478V}, which contains a mutated MHD motif leading to sensor-independent cell death. Most of these mutations also completely impair NRC4^{D478V}-mediated cell death, with the exception of L121E. While the NRC4^{L121E} mutation failed to induce cell death when co-expressed with Rpi-blb2/AVRblb2, NRC4$^{L121E/D478V}$ induced strong cell death (Fig. 1C). This suggests that residue L121 may play a role in the cooperation between NRC4 and its sensor NLRs. As we decided to focus on intrinsic features of the NRC4 CC domain, we excluded L121 from further analyses. In summary, we identified six key hydrophobic residues in helices α2 to α4 of the CC domain that contribute to NRC4-mediated cell death.

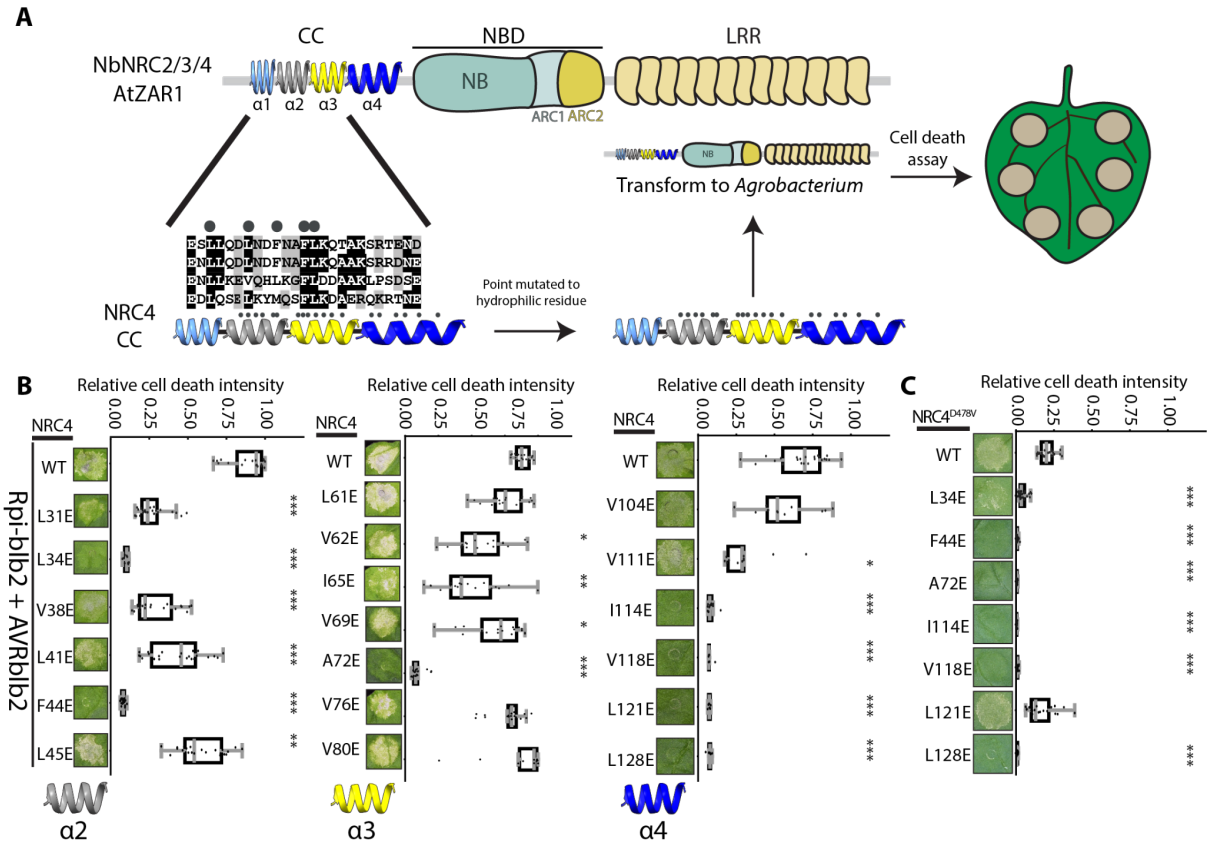

Figure 1. Mutation of conserved hydrophobic residues in the CC domain affects the cell death activity of NRC4. (A) Experimental design for screening key hydrophobic residues in the NRC4 CC domain. Conserved hydrophobic residues shared by NRC2/3/4 and AtZAR1 were selected and mutated to glutamic acid. The generated NRC4 variants were then tested in cell death assays. (B) Cell death assays of NRC4 hydrophobic variants, co-expressed with Rpi-blb2 and AVRblb2 in *nrc2/3/4*_KO *N. benthamiana*. Cell death intensity and phenotypes were recorded at 6 days post-infiltration (dpi). (C) Cell death assays of autoactive NRC4 variants with candidate hydrophobic residue mutations identified in panel B. For all cell death assays, the central line in each box plot represents the median cell death intensity, with box edges indicating the 25th and 75th percentiles. The whiskers extend to the most extreme data points no more than 1.5 x of the interquartile range.

Statistical differences between wild-type and variant samples were analyzed using the paired Wilcoxon signed rank test (*=p<0.01, **=p<0.005, ***=p<0.00001).

The identified residues form a hydrophobic Core in the CC domain

Using NRC2 (PDB: 8RFH) as a reference, we employed Alphafold3 (AF3) to model the dimer structure of NRC4, including the CC domain that was not captured in the original NRC2 cryo-EM data (Fig. 2, S3, and S4). We discovered that four of the identified residues (L34/A72/I114/V118) are located in proximity to each other, likely forming a hydrophobic core within the CC domain (Fig. 2A and S3). In contrast, the two other residues, F44 of α2 and L128 of α4, are positioned near each other but distant from the hydrophobic core (Fig. 2A).

Analysis of the predicted model revealed that the pairwise distances between the four residues in the hydrophobic core are less than 6Å, indicating potential interactions among them (Fig. 2B). Furthermore, the hydrophobic core is predicted to be concealed by the α1 helix in the resting state (Fig. 2C). Interestingly, the predicted distances from L34 and A72 to L13 of α1, a critical residue in the MADA motif, are within 6Å, suggesting potential interaction between the hydrophobic core and the MADA motif (Fig. 2C). These observations imply that this hydrophobic core within the CC domain may play a role in NRC4 function by interacting with the MADA motif.

In the activated state, NRC4 forms a hexameric resistosome (Liu *et al*, 2024). Our AF3 structural analysis reveals that the identified hydrophobic core is embedded within the CC domain inside the activated resistosome complex (Fig. 2D). In addition, F44 and L128, the two residues not part of the hydrophobic core, are localized near the putative ion-conducting pore within the resistosome. Furthermore, one of the residues in the hydrophobic core, A72 of the α3 helix, is positioned just one residue upstream of the EDVID motif (Fig. S3B), which interacts with the R-cluster in the LRR domain to ensure proper NRC4 function (Liu *et al*, 2024). Collectively, our structural analysis suggests that this hydrophobic core in the NRC4 CC domain might play a role in maintaining the structural integrity necessary for intramolecular interactions among different functional motifs, thereby regulating NRC4 activation.

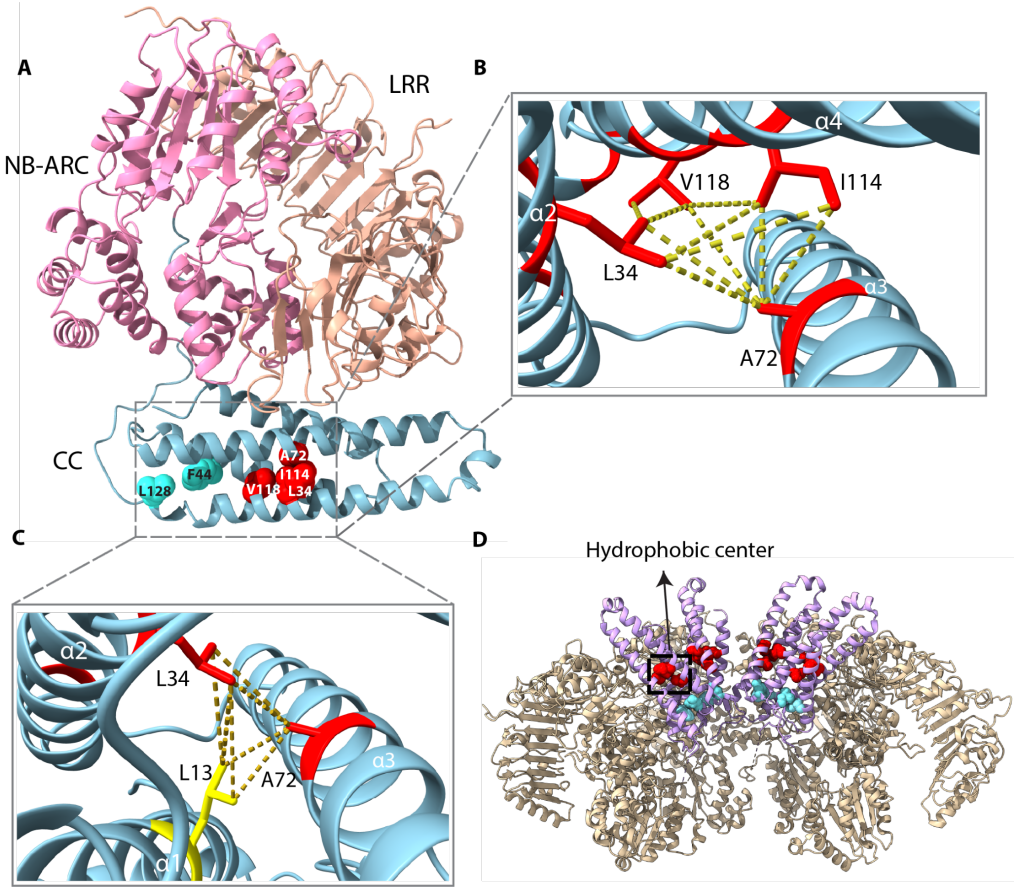

Figure 2. Four of the identified residues form a hydrophobic core at the center of the NRC4 CC domain. (A) The predicted NRC4 structure at the resting state. The coiled-coil (CC) domain is shown in light blue, the NB-ARC domain in pink, and the LRR domain in beige. The four residues that form the hydrophobic core are highlighted in red. The two other residues that are critical for NRC4 function but distant from the hydrophobic core, F44 and L128, are highlighted in cyan. (B) Close-up view of the hydrophobic core formed by L34, A72, I114, and V118 (red). Dashed lines indicate interactions where side-chain distances are less than 6 Å. (C) Spatial relationship between the hydrophobic core residues (red) and L13 (yellow) of the MADA motif in the α1 helix. Dashed lines represent potential interactions where side-chain distances are less than 6 Å. (D) The location of the hydrophobic core within the NRC4 resistosome (PDB: 9CC8). For clarity, only four of the six NRC4 protomers are displayed. The CC domains are shown in purple, with the remaining regions in gold. Hydrophobic core residues are highlighted in red, while F44 and L128 (residues outside the core) are indicated in cyan. All molecular structures (AlphaFold3-predicted models or PDB structures) were visualized using ChimeraX.

The hydrophobic core is essential for NRC4 subcellular localization and membrane-associated puncta formation

NRC4 localizes in the cytoplasm in its resting state, and forms membrane-associated puncta upon activation (Duggan *et al*, 2021). To investigate whether the hydrophobic core contributes to NRC4

220 subcellular localization in both resting and activated states, we tagged NRC4 variants with a C-
221 terminal GFP tag and performed cell biology experiments. Since wild-type NRC4 induces fast and
222 robust cell death, limiting its application in cell biology studies, we employed the NRC4$^{L9A/V10A/L14A}$
223 variant (NRC4^{AAA}) that carries mutations in the MADA motif (Adachi *et al*, 2019a). This variant
224 displays weaker and delayed cell death responses, allowing more accurate cell biology analysis (Fig.
225 S5). We therefore used the NRC4^{AAA} variant as the background for subsequent functional analyses.
226
227 To investigate subcellular localization in the resting state, we co-expressed NRC4 variants with Rpi-
228 blb2. We observed that the NRC4^{AAA} variant predominantly localized in the cytosol, consistent with
229 previously reported localization of wild-type NRC4 (Fig. S6) (Duggan *et al*, 2021; Wang *et al*, 2023).
230 Similarly, all four hydrophobic core mutants (L34E, A72E, I114E, and V118E) also predominantly
231 localized in the cytosol at the resting state, indicating that mutations in the hydrophobic core do not
232 affect NRC4 localization in the resting state (Fig. S6).
233
234 To determine whether the hydrophobic core affects NRC4 localization upon activation, we co-
235 expressed the NRC4 mutants with Rpi-blb2 and its recognized effector AVRblb2. Upon activation,
236 the NRC4^{AAA} variant exhibited a dramatic change in subcellular localization, forming membrane-
237 associated puncta (Fig. 3A), consistent with the previous finding for the NRC4^{L9E} variant (Duggan *et*
238 *al*, 2021). Interestingly, hydrophobic core mutants remained predominantly cytosolic when co-
239 expressed with Rpi-blb2 and AVRblb2, suggesting that these mutations impair the ability of NRC4 to
240 undergo activation-induced relocalization (Fig. 3A). However, the A72E mutant could still form a
241 limited number of membrane-associated punctate structures upon Rpi-blb2 activation (Fig. 3A). We
242 quantified cells with NRC4^{AAA} and NRC4^{A72E} puncta at 2 and 3 days post-infiltration (dpi) and found
243 that NRC4^{A72E} exhibited delayed punctate formation (Fig. S7A). These findings suggest that
244 NRC4^{A72E} has reduced efficiency and requires more time to oligomerize than NRC4^{AAA}. Collectively,
245 our results indicate that the hydrophobic core is essential for the efficient formation of NRC4
246 membrane-associated puncta upon activation of Rpi-blb2.
247
248 **Mutation of the hydrophobic core compromises NRC4 oligomerization**
249 NRC4 oligomerizes into a hexameric resistosome upon activation (Contreras *et al*, 2023b; Liu *et al*,
250 2024). To determine whether mutations in the hydrophobic core affect NRC4 oligomerization, we
251 conducted the Blue Native polyacrylamide gel electrophoresis (BN-PAGE) analysis using C-terminal
252 Myc-tagged NRC4 variants. NRC4 and Rpi-blb2 were co-expressed with or without AVRblb2, and
253 total proteins were collected for BN-PAGE analysis at 2 dpi. Consistent with previous reports using
254 NRC4^{L9E}, we observed that NRC4^{AAA} migrates as a ~240 kDa complex at the resting state, and forms
255 a ~900 kDa complex at the activated state (Fig. 3B) (Contreras *et al*, 2023b). Importantly, we found
256 that mutations in the hydrophobic core disrupted oligomerization, maintaining NRC4 in a dimeric

257 state even in the presence of both AVRblb2 and Rpi-blb2 (Fig. 3B). Additionally, the NRC4^{A72E}
258 mutant retained the ability to oligomerize at 3 dpi, forming a ~900 kDa band similar to NRC4^{AAA}
259 upon activation (Fig. S7B), consistent with its delayed puncta formation observed in microscopy.
260 Collectively, these results demonstrate that the hydrophobic core plays a critical role in NRC4
261 oligomerization, providing a structural basis for its essential function in NRC4-mediated immunity.
262

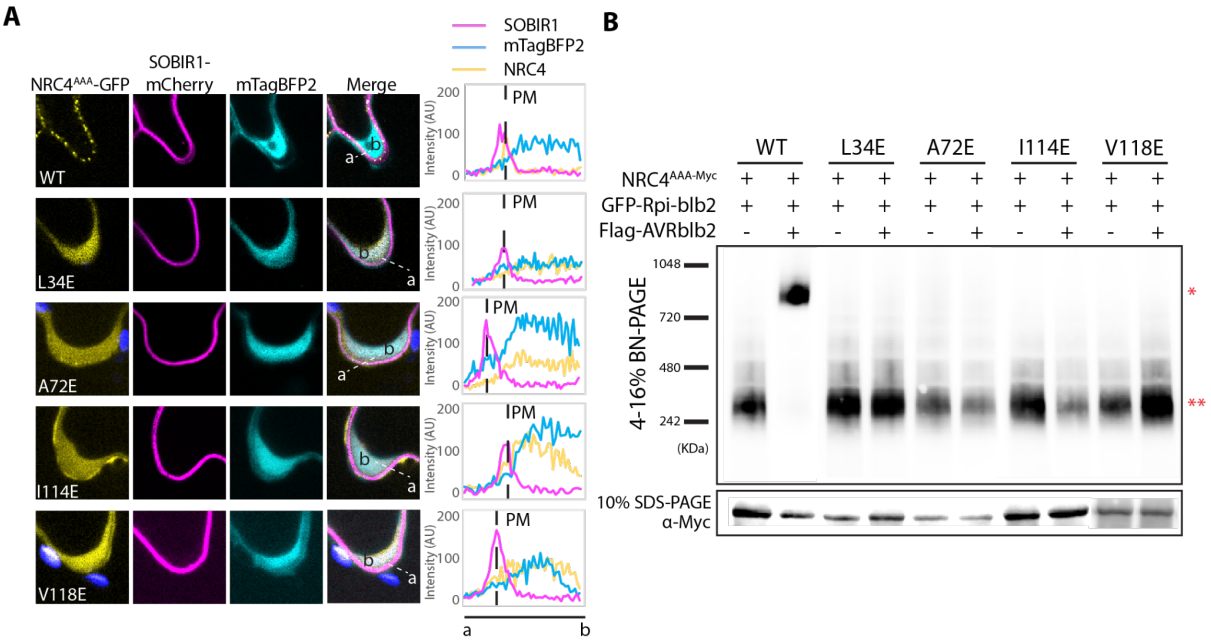

263
264 **Figure 3. Mutations in the hydrophobic core disrupted NRC4 puncta formation and**
265 **oligomerization.** (A) Confocal images showing subcellular localization of transiently-expressed GFP-
266 tagged NRC4^{AAA} and hydrophobic core mutants co-expressed with SOBIR1-mCherry (plasma
267 membrane marker) and mTagBFP2 (cytosol marker) in *nrc2/3/4*_KO *N. benthamiana* leaves that also
268 co-express Rpi-blb2 and AVRblb2. Images were captured at 2 dpi. The lines in the overlay panel
269 indicate the region selected for measuring the fluorescence intensity of each channel. The blue signal
270 corresponds to the chloroplast. The intensity was measured from position "a" to "b," and values are
271 reported in arbitrary units (AU). (B) Upper panel: BN-PAGE analysis showing the formation of the
272 NRC4^{AAA} and hydrophobic core mutant resistosomes. NRC4 variants and Rpi-blb2 were transiently
273 expressed in *nrc2/3/4*_KO *N. benthamiana* leaves, with and without AVRblb2. Lower panel: Western
274 blot analysis of SDS-PAGE to confirm NRC4 protein expression levels. Total protein samples were
275 collected at 2 dpi for both BN-PAGE and SDS-PAGE. Approximate molecular weights (kDa) are
276 indicated on the left. A single asterisk (*) indicates the NRC4 resistosome, while a double asterisk (**)
277 denotes the NRC4 dimer in the BN-PAGE data.
278
279 **The hydrophobic core contributes to the NRC4-phospholipid association**
280 A previous study demonstrated that five residues (K84, K87, K89, K91, and R94) within the
281 disordered region of the NRC4 CC domain play a role in its association with phospholipids (Wang *et*

282 *al*, 2023). To explore whether residues in the hydrophobic core also contribute to NRC4-phospholipid
283 interactions, we performed phospholipid-binding assays using PIP strips. We conducted wheat-based
284 *in vitro* translation to express the CC domain of $NRC4^{AAA}$ and corresponding hydrophobic core
285 mutants (Fig. 4A). After confirming protein accumulation, we incubated the proteins with PIP strips
286 to determine the association between the NRC4 CC domain and various phospholipids. The
287 fluorescent protein mCherry was used as a negative control to assess background binding.
288
289 We found that the $NRC4^{AAA}$ CC domain is associated with PI4P and $PI(4,5)P_2$, consistent with
290 previous reports using the wild-type NRC4 CC domain (Fig. 4B) (Wang *et al*, 2023). Additionally, we
291 observed the binding of $NRC4^{AAA}$ to other phospholipids, including PI-monophosphates (PI3P, PI5P),
292 PI-biphosphates [PI(3,4)P2, PI(3,5)P2], phosphatidic acid (PA) and phosphatidylserine (PS) (Fig. 4B).
293 However, we noted that the negative control mCherry also binds to PA and PS, suggesting that signals
294 detected with these lipids likely represent background binding in our assay.
295
296 In contrast, all variants harboring mutations in the hydrophobic core showed a substantially reduced
297 ability to bind either the mono- or biphosphate forms of PI (Fig. 4B). All hydrophobic core mutants
298 exhibited detectable protein accumulation levels, although variants A72E and I118E showed reduced
299 accumulation (Fig. 4B). We next examined the lipid-binding ability of the two variants carrying
300 mutations outside the hydrophobic core (F44E and L128E), both of which impaired NRC4-mediated
301 cell death (Fig. S8). Interestingly, these mutations did not affect the interaction of the NRC4 CC
302 domain with phospholipids (Fig. S8). Overall, our findings indicate that residues within the
303 hydrophobic core are indispensable for NRC4-phospholipid association, whereas residues outside the
304 core, such as F44 and L128, do not contribute to this association.
305
306 To further investigate the role of the hydrophobic core in membrane association, we conducted cell
307 fractionation assays to assess how mutations in this region influence the membrane localization of
308 full-length NRC4 under both resting conditions and upon activation. Under resting conditions,
309 $NRC4^{AAA}$ was detected in both soluble and membrane fractions at comparable levels (Fig. 4C). Upon
310 activation with Rpi-blb2/AVRblb2, $NRC4^{AAA}$ became significantly enriched in the membrane fraction,
311 consistent with previous findings (Fig. 4D) (Duggan *et al*, 2021). However, in contrast to $NRC4^{AAA}$,
312 the hydrophobic core mutants failed to exhibit enhanced membrane association upon activation with
313 Rpi-blb2/AVRblb2 (Fig. 4D). These results reveal that the hydrophobic core is important for NRC4-
314 phospholipid association and NRC4 membrane enrichment, corresponding to the cell biology
315 observations showing that the hydrophobic core of NRC4 is essential for its membrane-associated
316 puncta formation and oligomerization upon activation by Rpi-blb2/AVRblb2 (Fig. 3).
317

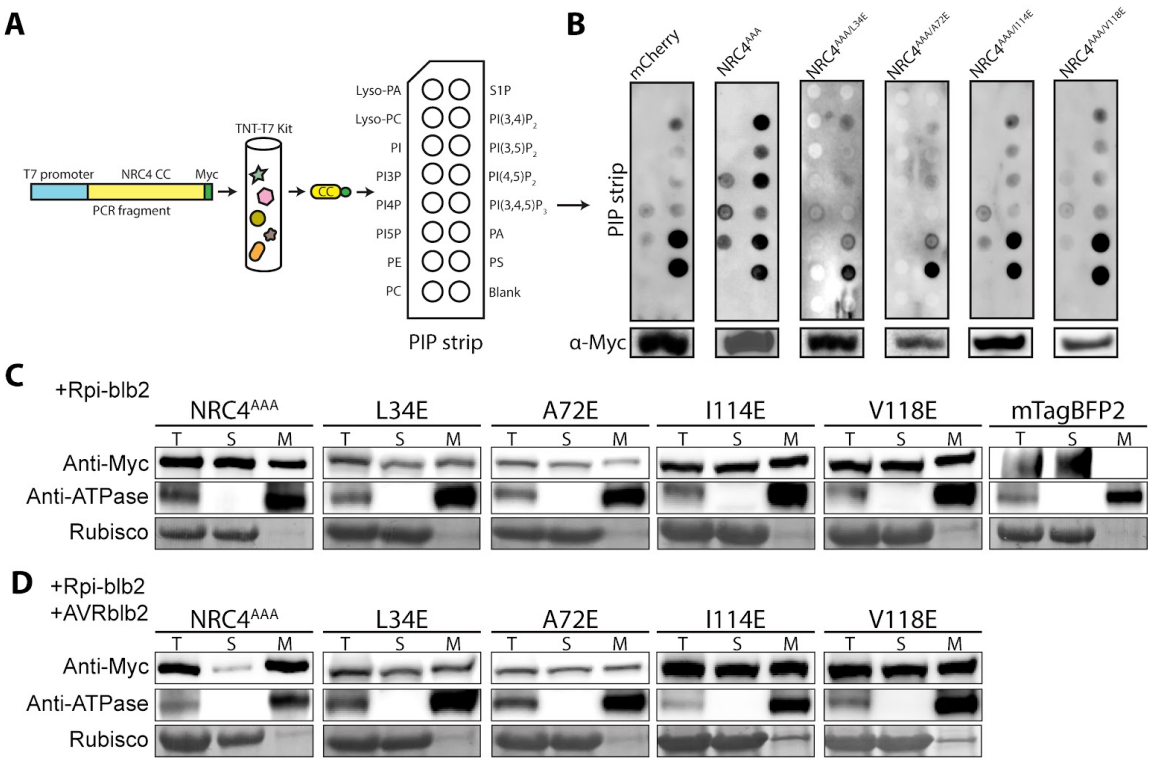

Figure 4. Mutations in the hydrophobic core compromise the NRC4 phospholipid association and membrane dynamics. (A) Experimental setup for investigating the association between the NRC4 CC domain and phospholipids. A gene fragment encoding the NRC4 CC domain with a C-terminal 4×Myc tag was amplified by PCR and *in vitro* translated using the TNT Coupled Wheat Germ Extract System. The resulting protein fractions were directly incubated with PIP strips for lipid association assays, and the NRC4 CC domain was detected using an anti-Myc antibody. (B) Phospholipid-binding assay for NRC4^{AAA} and hydrophobic core mutants. Myc-tagged mCherry served as a negative control. Expression levels of the *in vitro*-translated NRC4 CC domain variants were confirmed by western blot (shown below the binding assay results). (C) and (D) Membrane fractionation assay assessing the subcellular distribution of NRC4^{AAA} and hydrophobic core mutants co-expressed with Rpi-blb2, in the absence (C) or presence (D) of AVRblb2. Leaf samples were collected at 2 dpi, and total protein extracts were separated into soluble (S) and membrane (M) fractions. NRC4 proteins were detected using anti-Myc antibody. ATPase served as the membrane marker, while Rubisco is enriched in the soluble protein fraction. T represents the total extract. Rubisco was visualized by Coomassie blue staining.

Disruption of the hydrophobic core does not affect NRC4 accumulation around the pathogen haustoria

NRC4 accumulates around the extrahaustorial membrane (EHM) of *P. infestans* during infection, likely facilitating effector detection (Duggan *et al*, 2021). To investigate whether residues in the hydrophobic core are important for NRC4 focal accumulation at the EHM, we expressed NRC4^{AAA} or

its hydrophobic core mutants in *nrc2/3/4_KO N. benthamiana* leaves. At 1 dpi, we inoculated the detached leaves with *P. infestans* zoospores and examined the localization of NRC4 variants 2 days after pathogen inoculation. Consistent with previous reports on NRC4^{WT}, NRC4^{AAA}-GFP is focally accumulated at the EHM (Fig. 5) (Duggan *et al*, 2021). Similarly, all tested NRC4 hydrophobic core mutants displayed sharp signals around the EHM, but not in the cytosol or at the plasma membrane (Fig. 5). To further validate these observations, we utilized the NRC4^{WT}-RFP as an EHM marker to validate the localization of the NRC4 mutants. Co-localization between the NRC4 hydrophobic core mutants and NRC4^{WT}-RFP was observed, demonstrating that mutations in the hydrophobic core do not impair the capacity for EHM focal accumulation (Fig. S9). These findings reveal an interesting functional separation: while the hydrophobic core in the NRC4 CC domain is critical for resistosome formation, oligomerization, and phospholipid binding, it is dispensable for NRC4 focal accumulation at the EHM during pathogen infection. This suggests that distinct structural features within NRC4 mediate its different subcellular localization patterns during immune activation versus pathogen challenge.

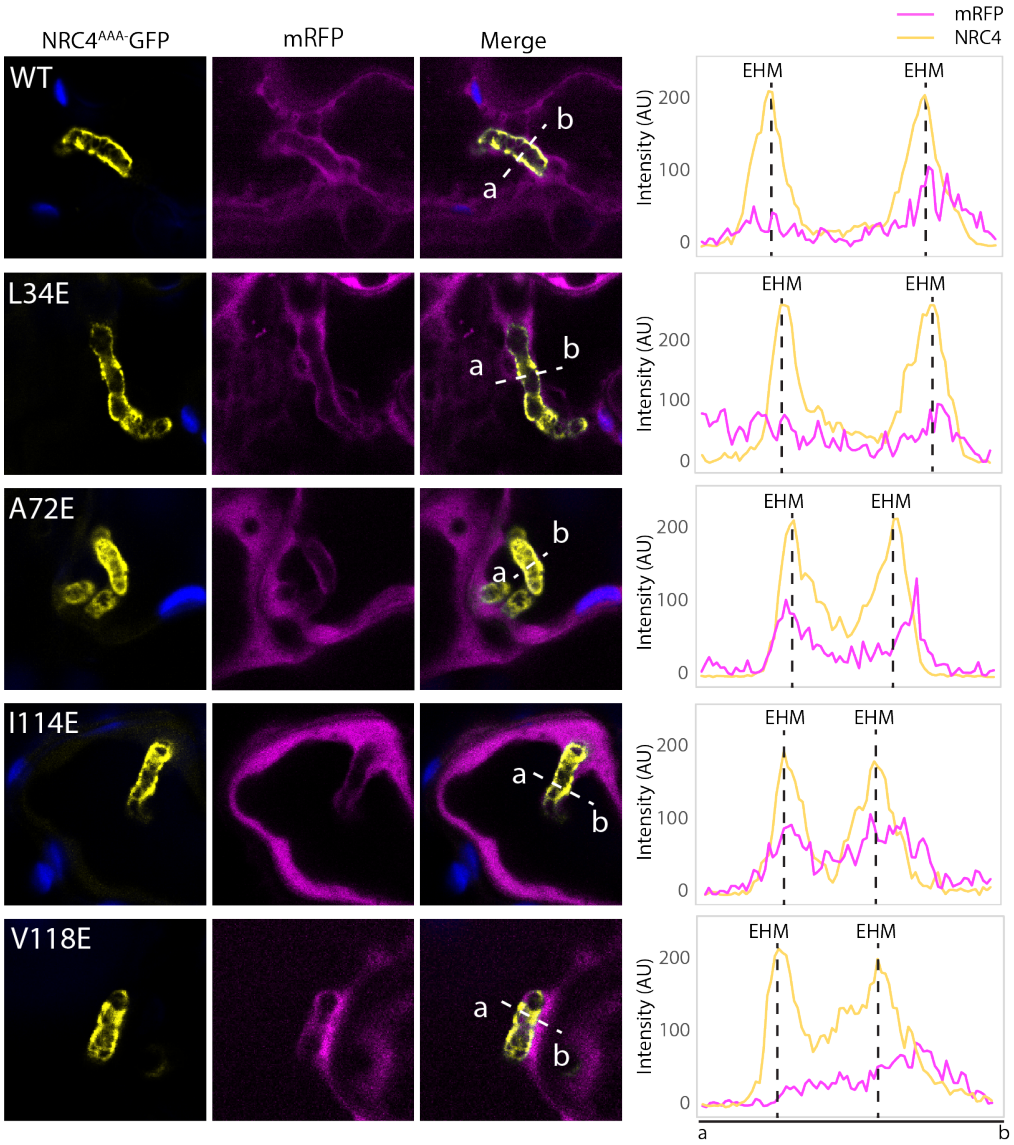

355 **Figure 5. Mutations in the hydrophobic core do not affect NRC4 focal accumulation at the**
356 **extrahaustorial membrane.** Confocal images showing the accumulation of NRC4^{AAA} and
357 hydrophobic core variants at the EHM. The NRC4 variants, tagged with C-terminal GFP, were
358 transiently expressed with mRFP (cytosol marker) in *nrc2/3/4_KO N. benthamiana* leaves. At 1 dpi, *P.*
359 *infestans* zoospores were inoculated onto detached leaves and incubated for two days. Images were
360 taken at 3 dpi. The lines marked on the overlay panel indicated the selected region for measuring the
361 intensity of each channel. The blue signal represents the chloroplast. Fluorescence intensity was
362 measured from position "a" to "b" in each group, and the values are presented as arbitrary units (AU).
363
364 **The hydrophobic core within the CC domain is critical for the function of NRC helper NLRs**
365 **and some singleton NLRs**
366 Our discovery of a novel functional feature in the CC domain prompted us to investigate its
367 conservation across other NLRs, focusing on those within the NRC superclade, as well as related
368 singleton CNLs ZAR1, R2, and Rpi-vnt1 (Figure 6A). We selected 22 species representing diverse
369 genera within the Solanaceae family from a recently published solanaceous NLRome dataset
370 (Sugihara *et al*, 2023). From this dataset, we extracted 2,797 NLR sequences and grouped them into
371 phylogenetic clades based on their NB-ARC domains (Fig. 6A, Fig. S10, File S1). Among these
372 NLRs, a significant proportion of sensor NLRs in the NRC superclade contain N-terminal extensions
373 that likely influence the canonical properties of the CC domain (Fig. S10) (Seong *et al*, 2020);
374 therefore, we excluded these sensor NLRs from further analysis. From the remaining clades in the
375 NRC superclade, we selected representative NLRs from each clade for detailed analysis: NRC2 from
376 G8 clade, Rx from G12 clade, Bs2 from G2 clade, Rpi-amr1 from G14 clade, and Rpi-amr3 from G9
377 clade (Fig. 6A).
378
379 To determine whether the hydrophobic core feature is present in selected NLR groups, we aligned the
380 CC domain sequences and identified the corresponding residues in each group (Files S2 to S9). These
381 residues were then highlighted on the AlphaFold3-predicted CC domain structures of selected
382 candidate NLRs. Fascinatingly, a compact hydrophobic core could be readily predicted in ZAR1, R2,
383 Rpi-vnt1.1, and NRC2. In contrast, all representative NRC-dependent sensor NLRs lacked a predicted
384 compact hydrophobic core (Fig. 6B). This pattern mirrors the absence of the MADA motif in these
385 sensor NLRs, suggesting that during evolution, both the hydrophobic core and the MADA motif
386 degenerated in NRC-dependent sensor NLRs. This finding further implies that the cell death-eliciting
387 function in NLRs depends on both the MADA motif and the hydrophobic core.
388
389 Next, we performed sequence conservation analysis on the NLRs that form a hydrophobic core. The
390 hydrophobic core residues in the G8 (NRC) clade were highly conserved, with most sequences
391 containing LAIV (Fig. 6C). Entropy analysis revealed that these residues had entropy values lower

392 than 0.75, signifying their relatively high sequence conservation (Fig. 6C). Similarly, the hydrophobic
393 core residues in ZAR1, G5 clade, and G11 clade were also highly conserved, predominantly featuring
394 LAII, LALI, and LVIV, respectively (Fig. 6C). Entropy analysis showed that the hydrophobic core
395 residues in the G5 and G11 clades have low entropy values, with the ZAR1 clade showing no
396 variation at these positions (Fig. 6C, Dataset S3, File S2).
397
398 To test whether the hydrophobic core is functionally conserved across these clades, we introduced
399 point mutations in each of the residues in the hydrophobic core of representative NLRs from each
400 clade. We first co-expressed wild-type NRC2 and its hydrophobic core mutants with Pto and effector
401 AvrPto, which leads to Prf- and NRC2-dependent cell death, in *nrc2/3/4_KO* plants. All point
402 mutations in the hydrophobic core of NRC2 compromised NRC2-mediated cell death, confirming the
403 importance of the hydrophobic core in both NRC2 function (Fig. 6D, Fig. S11 A, B).
404
405 We then tested the functional importance of the hydrophobic core residues in ZAR1, R2 from G5
406 clade, and Rpi-vnt1 from G11 clade. For ZAR1 assays, we utilized the autoactive mutant $ZAR1^{D481V}$
407 to elicit cell death. Cell death assays demonstrated that all hydrophobic core mutations in $ZAR1^{D481V}$
408 significantly compromised its ability to mediate hypersensitive cell death, underscoring the critical
409 role of the hydrophobic core in ZAR1 function (Fig. 6D, Fig. S11C, D). For Rpi-vnt1.1, we co-
410 expressed Rpi-vnt1 or its hydrophobic core mutants with its cognate effector AVRvnt1 to elicit Rpi-
411 vnt1.1-dependent cell death. Similar to $ZAR1^{D481V}$, all the hydrophobic core mutants of Rpi-vnt1
412 compromised the cell death function of this NLR.
413
414 We then co-expressed wild-type R2 with its cognate effector AVR2 and observed strong
415 hypersensitive cell death. Interestingly, while hydrophobic core mutants V72E and I117E
416 significantly compromised R2 cell death function, the mutants L34E and L113E continued to exhibit
417 strong cell death comparable to wild-type R2, suggesting that certain hydrophobic core residues in R2
418 may have functionally degenerated. Notably, R2 lacks the functional EDVID motif at the α3 helix
419 (Fig. 6B, S12), unlike other tested candidate NLRs, implying that the presence of the EDVID motif is
420 critical for the proper functional importance of the hydrophobic core in CNLs.
421
422 Altogether, our structural and functional analyses demonstrate that NRC helper NLRs and some
423 singleton NLRs contain a compact hydrophobic core feature in the CC domain that is critical for NLR
424 function. Additionally, the presence of both the MADA motif and the EDVID motif appears essential
425 for the full functional significance of this hydrophobic core (Fig. 6B, D). As the hydrophobic core is
426 strategically positioned between these two important functional motifs, we propose that these
427 structural elements cooperate to execute the hypersensitive cell death-eliciting function of NLRs.
428

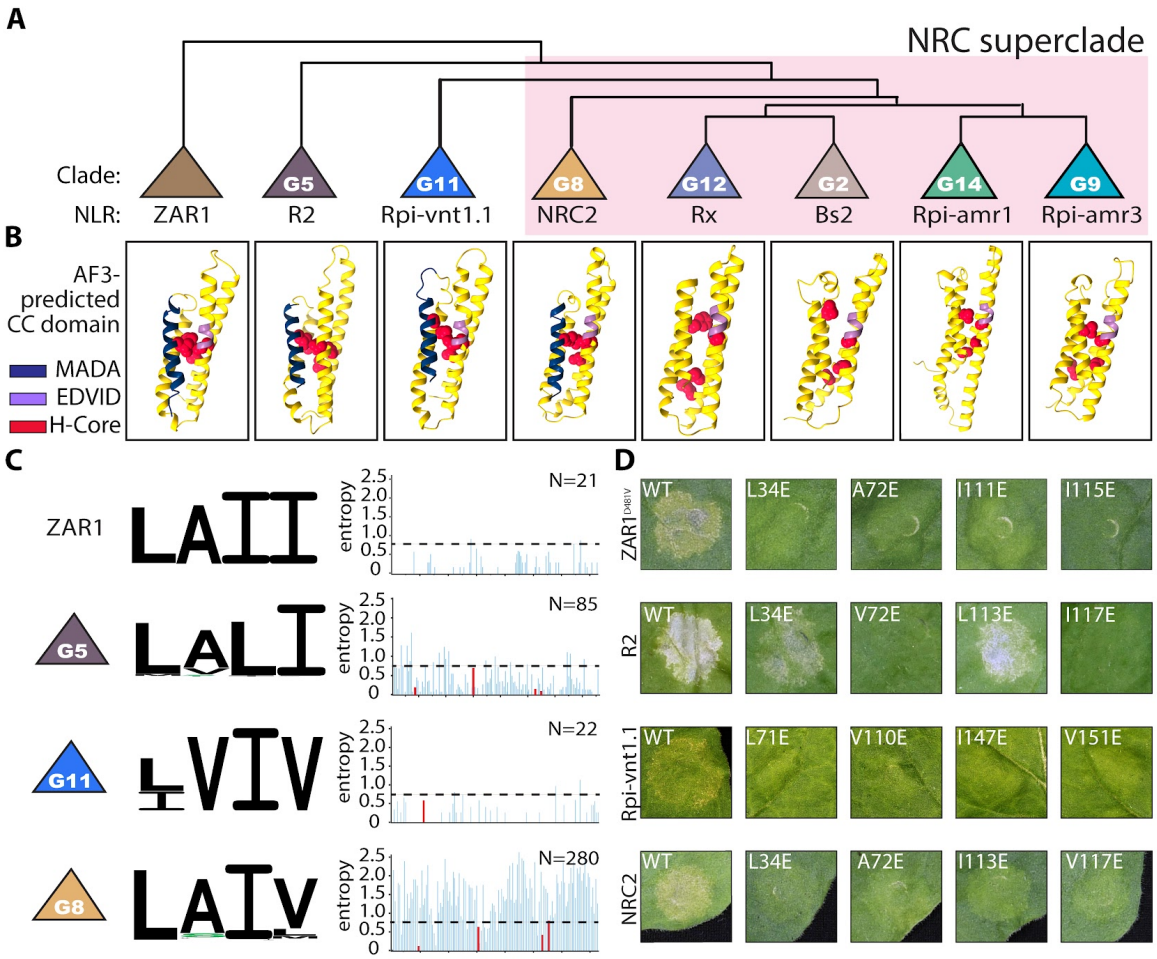

Figure 6. The hydrophobic core in the CC domain is essential for NRC2, ZAR1, and Rpi-vnt1.1. (A) Phylogenetic tree of the NRC superclade and related singleton NLRs, ZAR1, R2 and Rpi-vnt1.1. A representative NLR is indicated for each group. The NRC superclade is highlighted in pink. Sensor NLR clades possessing N-terminal extensions were excluded from this analysis. (B) AlphaFold3-predicted structures of selected NLRs. Red indicates hydrophobic core residues obtained from 2D alignment. H-Core represents the hydrophobic core. Blue indicates the MADA motif, and purple indicates the EDVID motif. (C) The amino acid composition of the hydrophobic core in each group is shown in the logo. Hydrophobic residues (AVLIPWFM) appear in black, hydrophilic residues (DE) in red, positively charged residues (KRH) in blue, and polar residues (STN) in green. From left to right, the positions correspond to NRC4 residues L34, A72, I114, and V118. Entropy values for the CC domain across singleton NLR ZAR1, R2, Rpi-vnt1.1, and NRC, with respective hydrophobic core residues in each clade highlighted in red. The number of NLR sequences in each clade is indicated in the top-right corner of the entropy panel. (D) Cell death phenotypes following hydrophobic core mutations in representative NLRs from each clade, photographed at 3 dpi. Quantitative data for these cell death assays can be found in Figure S11.

Discussion

447 While recent cryo-EM studies unveiled detailed structures of NRC complexes in both resting and
448 activated states, the precise structural features of the CC domain were not fully resolved, likely due to
449 the high flexibility of the region connecting the CC and NB-ARC domains (Liu *et al*, 2024;
450 Madhuprakash *et al*, 2024; Selvaraj *et al*, 2024). Building upon the previously established knowledge
451 of the MADA motif in the α1 helix, our study identified several conserved hydrophobic residues
452 across NRCs within the α2 to α4 helices (Fig. S1). We further demonstrated that several of these
453 hydrophobic residues, situated at the core of the CC domain, form a hydrophobic core essential for
454 NRC4 function (Fig. 1 and 2).
455
456 Several CNL-type singleton and helper NLRs undergo dynamic subcellular transitions from the
457 cytosol to the plasma membrane, where they form pentameric or hexameric resistosome complexes
458 upon activation (Wang *et al*, 2019a; Bi *et al*, 2021; Duggan *et al*, 2021; Liu *et al*, 2024). We found
459 that mutations in the hydrophobic core do not affect the subcellular dynamics of NRC4 in its resting
460 state (Fig. S6). However, upon activation of the sensor NLR Rpi-blb2, these mutations hinder the
461 ability of NRC4 to oligomerize and localize to the plasma membrane (Fig. 3A). Additionally, BN-
462 PAGE analysis showed that the hydrophobic core mutants remain as dimers when co-expressed with
463 Rpi-blb2 and AVRblb2 (Fig. 3B). One possible explanation is that NRC4 hydrophobic core mutants
464 are unable to receive activation signals from sensor NLRs, remaining as inactive homodimers in the
465 cytosol. Alternatively, the hydrophobic core mutant NRC4 can receive the signal, but the mutation
466 altered the CC domain structure, preventing the disruption of the homodimer and the formation of
467 resistosome complexes.
468
469 While the MADA motif is an essential feature in the α1 helix of NRC4, the detailed mechanism of
470 how hydrophobic residues in the MADA motif contribute to NRC4 function remains unclear (Adachi
471 *et al*, 2019a). Using AF3 predictions, we showed that the L13 residue within the MADA motif, which
472 is critical for NRC4 cell death activity, potentially interacts with two hydrophobic core residues in the
473 α2 and α3 helices (Fig. 2C). The ZAR1 resistosome study proposed a "flipping out" process of the α1
474 helix in the CC domain during ZAR1 activation, a crucial event for ZAR1-mediated cell death (Wang
475 *et al*, 2019a). Prior structural analysis of NRCs failed to identify the α1 helix of the CC domain in the
476 activated resistosome, suggesting that this helix might also undergo the "flipping out" process (Liu *et*
477 *al*, 2024; Madhuprakash *et al*, 2024). Given the similarity between ZAR1 and NRC resistosomes, we
478 speculate that mutations in this hydrophobic core could disrupt interactions between the MADA motif
479 and the α2-α3 helices, impairing the "flipping-out" process of the α1 helix during activation and
480 ultimately compromising ZAR1 and NRC function.
481
482 A recent cryo-EM study showed that a triple mutation within the EDVID motif of the α3 helix
483 disrupts NRC4-mediated cell death, while single mutations in this region do not affect NRC4

484 functionality (Liu *et al*, 2024). In contrast, we observed that a single mutation at A72, located adjacent
485 to the conserved EDVID motif in the hydrophobic core, is sufficient to impair NRC4-mediated cell
486 death (Fig. 1C). Interestingly, NRC4 with the A72 mutation can still oligomerize and localize to the
487 plasma membrane at 3 dpi. However, the A72E mutant resistosome is non-functional and unable to
488 trigger cell death. Our findings suggest that A72 likely plays a role in modulating interactions
489 between the EDVID motif and the R-cluster, thus regulating NRC4-mediated cell death (Fig. 1C, Fig.
490 S3B).
491
492 The interaction between phospholipids and helper NLRs is crucial for NLR-mediated cell death (Saile
493 *et al*, 2021; Wang *et al*, 2023). NRC4 has previously been shown to associate with PI4P and PI(4,5)P_2,
494 two key phospholipids located on the plasma membrane (Wang *et al*, 2023). A positively charged
495 cluster in the α4 helix of NRC4, conserved among other helper NLRs such as ADR1 and NRG1, plays
496 a vital role in NRC4-phospholipid interaction (Wang *et al*, 2023). In our study, single mutations in the
497 hydrophobic core of NRC4 disrupted its association with phospholipids (Fig. 4B). Since the
498 hydrophobic core is embedded within the resistosome, it is unlikely to interact directly with lipids in
499 the activated state (Fig. 2D). A possible explanation is that these mutations alter the structure of the
500 NRC4 CC domain, disrupting the proper conformation of the positively charged loop and thereby
501 impairing interactions between NRC4 and phospholipids. Notably, most hydrophobic core mutants of
502 NRC4 lose both their capacity to associate with phospholipids and their ability to oligomerize. Our
503 results support the hypothesis that NRC4-phospholipid interactions are crucial for resistosome
504 formation. When the CC domain structure is disrupted, NRC4-phospholipid binding is compromised,
505 causing NRC4 to remain in a cytosolic homodimer state rather than oligomerizing into functional
506 resistosome complexes (Fig. 3 and 4).
507
508 The focal accumulation of NRC4 on the EHM is a distinctive feature observed during *P. infestans*
509 infection (Duggan *et al*, 2021). Interestingly, NRC4 hydrophobic core mutants can still focally
510 accumulate on the EHM during infection, indicating that these mutations do not affect all intrinsic
511 features of NRC4. Previous studies on phospholipid composition at the EHM identified PI4P and
512 PI(4,5)P_2 as the primary phospholipids enriched at the EHM (Rausche *et al*, 2021). However, our
513 lipid-binding assay reveals that hydrophobic core mutations of NRC4 abolish the ability to associate
514 with both PI4P and PI(4,5)P_2 (Fig. 4B). One possible explanation is that the focal accumulation of
515 NRC4 on the EHM may not depend on direct association of the NRC4 CC domain with lipids. Instead,
516 other regions of the NRC4 canonical domain or interactions with host or pathogen proteins are likely
517 involved in this process. NRC4 may require these additional domains or partnering proteins to
518 facilitate NRC4 focal accumulation on the EHM.
519

Previous studies suggest that NRC helper NLRs and NRC-dependent sensor NLRs arose through sub-functionalization from an ancestral singleton NLR (Contreras *et al*, 2023a). This process likely involved divergence of sequence features, resulting in altered protein functionality. One notable example is the MADA motif, which is conserved among NRCs, ZAR1, and some sensor NLRs, but not in NRC-dependent sensor NLRs (Adachi *et al*, 2019a). Similarly, while the hydrophobic core described here is conserved in some singleton CNLs and NRC helper NLRs, it is missing in NRC-dependent sensor NLRs (Fig. 6B). We propose that together with the MADA motif, the hydrophobic core emerged in the common ancestral NLR of singleton CNLs and NRC helper NLRs, but subsequently degenerated in NRC-dependent sensor NLRs.

Although the hydrophobic core is present in R2, only two of the mutants demonstrated reduced cell death (Fig. 6D). In both ZAR1 and NRCs, activation triggers the formation of pentameric or hexameric resistosomes, which initiate downstream hypersensitive responses (Wang *et al*, 2019a; Madhuprakash *et al*, 2024; Liu *et al*, 2024). However, it remains unclear whether R2 forms a resistosome similar to those of NRCs or ZAR1 and induces cell death through a comparable mechanism. Notably, R2 contains the MADA motif, which is critical for cell death initiation in many NLRs. In contrast, the EDVID motif—a conserved feature found in ZAR1, Rpi-vnt1.1, NRCs, and many other NLRs—is absent in R2 (Fig. 6B, S12) (Förderer *et al*, 2022; Rairdan *et al*, 2008; Wróblewski *et al*, 2018). The presence or absence of MADA and EDVID motifs, coupled with the variable requirement for the hydrophobic core described here, suggests that different types of CNLs possess unique structural and sequence features within their CC domains, resulting in distinct regulatory mechanisms (Fig. 6).

In conclusion, our study identifies a previously uncharacterized hydrophobic core in the CC domain of NRC helper NLRs and some singleton NLRs that is essential for their functions in immune signaling. This hydrophobic core contributes to resistosome formation, phospholipid binding, and subcellular dynamics, but is dispensable for NRC4 focal accumulation at the EHM during pathogen infection. Furthermore, our analysis reveals that this structural feature is highly conserved in NRC helper NLRs and some singleton NLRs but has diverged in sensor NLRs, providing new insights into the structure-function connection of NLR-mediated immunity in plants.

557 **Materials and Methods**

558

559 **Plant material and growth conditions**

560 Wild-type and *nrc2/3/4_KO N. benthamiana* plants were grown in a walk-in growth chamber
561 maintained at 25 ºC, under a 16 h light/8 h dark cycle (Wu *et al*, 2020).

562

563 **Plasmid construction**

564 The CC, NB-ARC, and LRR domains of NRC2/4 were modularized and cloned into the Golden Gate
565 Level 0 acceptor vector pAGM9121 (Weber *et al*, 2011). Site-directed mutagenesis were performed
566 on the CC domain Level 0 module using inverse PCR, and then digested with AarI (NEB) and ligated
567 with T4 DNA ligase (Thermo Scientific). The mutated CC domain modules were assembled with the
568 NB-ARC and LRR modules, along with a C-terminal 4x Myc tag or GFP tag, into the pICH86988
569 binary vector, containing the 35S promoter and OCS terminator, using Golden Gate assembly (Weber
570 *et al*, 2011; Engler *et al*, 2014). The pICH86988 constructs containing NRC4-myc or GFP were
571 subsequently transformed into *Agrobacterium tumefaciens* strain GV3101(pMP90). For *in vitro*
572 translation experiments, the CC domain module of NRC4 (wild-type and hydrophobic core mutants)
573 was assembled with the T7 promoter, CMV1 5' UTR, T7 terminator, and an overhang-modified C-
574 terminal Myc tag (CTCA-GCTT) into the acceptor vector pICSL86900OD (Engler *et al*, 2014). To
575 study the hydrophobic core function in R2 and Rpi-vnt1.1, the CDS of R2 and Rpi-vnt1.1 were cloned
576 into Level 0 acceptor pAGM9121(Tai *et al*, 1999; Foster *et al*, 2009). For ZAR1, a D481V mutation
577 variant (autoactive) Level 0 plasmid was used (Contreras *et al*, 2024). Site-directed mutagenesis in the
578 CC domain was performed as described above. The resulting NLR variants were subcloned into
579 pICH86988 for cell death assays. The effector gene AVR2 was synthesized and assembled into
580 pICH47751 vectors, incorporating the 35S promoter and OCS terminator (Gilroy *et al*, 2007; Lin *et al*,
581 2022). The primers used for cloning and the plasmids used in this study are listed in Datasets S1 and
582 S2.

583

584 **Agroinfiltration**

585 *A. tumefaciens* GV3101(pMP90) was used to express NLRs and effectors. The *Agrobacterium* stocks
586 were refreshed on 523 medium containing the appropriate antibiotics and incubated overnight at 28°C.
587 The cells were harvested by centrifugation at 5000 × g for 5 minutes and resuspended in MMA buffer
588 (10 mM $MgCl_2$, 10 mM MES-KOH, 150 μM acetosyringone, pH 5.6). The cell concentrations were
589 adjusted to 0.2 for all NLRs and 0.1 for all effectors for subsequent experiments. *Agrobacterium*
590 suspensions with the desired optical density (OD) were infiltrated into *N. benthamiana* leaves using a
591 1 mL syringe.

592

593 **Cell death assay**

594 The complementation assays were performed in the *nrc2/3/4*_KO *N. benthamiana*, while functional
595 analyses of hydrophobic core-mutated R2, ZAR1, and Rpi-vnt1.1 were conducted in wild-type *N.*
596 *benthamiana*. The NLR proteins and their corresponding effectors were transiently expressed in *N.*
597 *benthamiana* using *A. tumefaciens* strains carrying expression vectors for the indicated proteins. Cell
598 death intensity was quantified using the UVP ChemStudio Imaging System (Analytik Jena) at 6 dpi
599 for NRC4 mutants screen and at 3 dpi for R2, ZAR1, NRC2/3, and Rpi-vnt1.1 mutants.
600 Autofluorescence of necrotic regions was detected using the blue LED excitation light and a FITC
601 emission filter (519 nm). Cell death intensity was normalized by dividing the pixel value by the
602 maximum signal pixel value (65535) detected by the UVP ChemStudio.
603
604 **Protein extraction for SDS-PAGE analysis**
605 The protein extraction method was conducted as previously described (Win *et al*, 2011). The leaf disc
606 was homogenized with ceramic beads in a tissue homogenizer under liquid nitrogen. Total protein
607 was extracted with GTEN buffer comprising 10% glycerol, 25 mM Tris (pH 7.5), 1 mM EDTA, 150
608 mM NaCl, 2% (w/v) PVPP, 10 mM DTT, 1× protease inhibitor cocktail (Sigma, P9599), and 0.2%
609 IGEPAL (Sigma). The protein extract was centrifuged at 5000 g for 10 minutes at 4ºC, and the
610 supernatant was transferred to a new Eppendorf tube and centrifuged again at 13000 ×g for 5 minutes
611 at 4 °C to remove the remaining debris as possible. The final supernatant was combined with 4x
612 sample loading dye containing 200 mM Tris-HCl (pH 6.8), 8% (w/v) SDS, 40% (v/v) glycerol, 50
613 mM EDTA, 0.08% bromophenol blue, and 0.1 M DTT. The protein samples were incubated at 70 ºC
614 for 10 minutes before SDS-PAGE analysis.
615
616 **SDS-PAGE assay and immunodetection analysis**
617 SDS-PAGE electrophoresis and immunodetection analyses were conducted as previously described
618 (Win *et al*, 2011). Denatured samples were separated on PAGE gels prepared with 10% or 15% T-Pro
619 EZ gel solution (Omics bio), containing 0.1% TEMED (Bio-Rad) and 0.1% ammonium persulfate
620 (Bio-Rad). Proteins were transferred to a PVDF membrane using the Trans-Blot Turbo Transfer
621 System (Bio-Rad). Following the transfer, the membrane was washed with Tris buffer saline (TBS)
622 with 0.1% Tween-20 and blocked with 5% nonfat dry milk. For immunodetection, anti-Myc
623 (GenScript, A00704) and anti-H+ATPase (Agrisera, AS07 260) were used as primary antibodies for
624 NRC4 protein and membrane fraction detection, respectively. Secondary antibodies included
625 Peroxidase AffiniPure Goat Anti-Mouse IgG (H+L) (Jackson, 115-035-003) and Peroxidase
626 Conjugated Goat Anti-Rabbit IgG (H+L) (Sigma, AP132P). Primary antibodies were diluted at
627 1:5000, and the secondary antibodies were diluted at 1:20000. Chemiluminescence signals were
628 detected using a mixture of SuperSignal West Pico PLUS Chemiluminescent Substrate (Thermo
629 Scientific, 34580) and SuperSignal West Femto Maximum Sensitivity Substrate (Thermo Scientific,

630 34096) in a 3:1 ratio. Images were captured using the UVP ChemStudio Imaging System. SimplyBlue
631 SafeStain (Invitrogen, 465034) was used to visualize the Rubisco signal on the PVDF membrane.
632
633 **Blue Native PAGE**
634 The BN-PAGE method was conducted as previously described (Contreras *et al*, 2023b). To assess
635 whether oligomerization was affected in the mutants, we transiently expressed the NRC4 hydrophobic
636 core mutants along with Rpi-blb2, with or without AVRblb2, in 4-week-old plants. Leaf discs were
637 collected at 2 and 3 dpi, and total protein was extracted using a native PAGE extraction buffer
638 containing 50 mM HEPES (pH 7.5), 50 mM NaCl, 5 mM MgCl2, 10% glycerol, 10 mM DTT, 1x
639 protease inhibitor cocktail (Sigma, P9599), and 1% digitonin (Sigma, D141). Protein extracts were
640 incubated on ice at 4 ºC for 10 minutes, followed by centrifugation at 12,000 rpm for 15 minutes at 4
641 ºC. The supernatant was transferred to a new tube and centrifuged again at 12,000 rpm for 10 minutes
642 at 4 ºC to avoid the interference of the pellet. The resulting protein extracts were diluted to 0.4x using
643 the native PAGE extraction buffer. Diluted samples were then mixed with 4x sample buffer and
644 NativePAGE 5% G-250 Sample Additive to achieve a final G-250 concentration of 0.125%. Samples
645 were loaded onto a 4–16% Native PAGE gel (Invitrogen, BN1002) and electrophoresis was carried
646 out following the manufacturer's protocol. In brief, Native PAGE was performed using the XCell
647 system (Invitrogen) at 4 ºC. The gel was run with a dark cathode buffer at 150 V for 45 minutes,
648 followed by replacing the dark cathode buffer with a light cathode buffer and continuing at 200 V for
649 120 minutes. After electrophoresis, proteins were transferred to a PVDF membrane using the Trans-
650 Blot Turbo Transfer System (Bio-Rad). The membrane was fixed with 8% acetic acid, air-dried in a
651 chemical hood, and subsequently rinsed with 99% ethanol. The membrane was washed with ddH_2O
652 and TBST to remove residual ethanol before the immunodetection mentioned above.
653
654 ***In vitro* translation**
655 The plasmid containing the *T7-CMV1:NRC4 CC-Myc* fragment was amplified using the T7 promoter
656 forward primer and the T7 terminator reverse primer with the KAPA HiFi HotStart ReadyMix
657 (Roche). The resulting PCR fragments were purified using a FavorPrep GEL/PCR purification Mini
658 kit (Favorgen). The *in vitro* translation assay was performed following the protocol of the TNT-T7
659 coupled wheat germ extract system (Promega). Briefly, 1 µg of purified PCR fragments was mixed
660 with the TNT wheat germ extract, TNT reaction buffer, amino acid mixture, RNase inhibitor, and T7
661 polymerase. The reaction mixture was incubated at 30ºC for 2 hours. The NRC4-CC domain tagged
662 with 4× Myc was subsequently analyzed by immunoblotting as mentioned above.
663
664 **Lipid binding assay**
665 The PIP strips (Invitrogen) were first blocked by incubating with 3% bovine serum albumin (Fraction
666 V, low heavy metal, MERK) at room temperature for one hour. The NRC4 CC domain proteins,

667 obtained from *in vitro* translation, were then incubated with the PIP strips at 4°C overnight. Following
668 incubation, the PIP strips were washed with TBST before the immunodetection assay as described
669 above.
670
671 **Protein fractionation**
672 Membrane enrichment was performed using a slightly modified version of a previously described
673 protocol (Abas & Luschnig, 2010). NRC4 was transiently co-expressed with *Rpi-blb2*, with or
674 without *AVRblb2*, in *nrc2/3/4_KO N. benthamiana*. At 2 dpi, leaves were harvested and homogenized
675 under liquid nitrogen using a pestle and mortar. The powdered leaf tissue was mixed with membrane
676 protein extraction buffer (0.33 M sucrose, 20 mM Tris-HCl [pH 8], 1 mM EDTA), supplemented with
677 5 mM DTT, 1× protease inhibitor (Thermo Scientific), and 0.5% PVPP. The mixture was first
678 centrifuged at 2000 ×g, and the supernatants were further filtered through Miracloth (MERK, 475855-
679 1R). The supernatant was transferred to a new Eppendorf tube, and 50 µl was set aside as the total
680 protein fraction. The remaining supernatant was ultracentrifuged at 21,000 ×g for 1.5 hours to
681 separate the soluble protein fraction and the membrane protein. The soluble protein fraction was
682 transferred to a new Eppendorf tube, while the pellet was resuspended in a membrane extraction
683 buffer (without PVPP) at one-third the volume of the soluble protein fraction. The membrane fraction
684 was then diluted threefold with a membrane extraction buffer (without PVPP) before being applied to
685 SDS-PAGE and immunoblotting analysis.
686
687 **Confocal microscopy**
688 To analyze the subcellular localization of wild-type and hydrophobic core-mutated NRC4, four-week-
689 old *nrc2/3/4_KO N. benthamiana* plants were agroinfiltrated with NRC4-GFP, HF-Rpi-blb2,
690 mTagBFP, SOBIR1-mCherry, and either with or without Flag-AVRblb2. At 2 or 3 dpi, discs of the
691 infiltrated leaves were imaged using an Andor Dragonfly spinning disc confocal microscope (Andor)
692 equipped with a 40× water immersion objective lens (Advanced optical microscope core facility,
693 Academia Sinica) or Leica Stellaris 8 inverted confocal microscope with 40x water immersion
694 objective lens (Live-cell-image core lab, Institute of Plant and Microbiology, Academia Sinica).
695 Excitation wavelengths of 405 nm, 488 nm, and 561 nm were used for BFP, GFP, and mCherry,
696 respectively. The corresponding emission wavelengths were 422–468 nm for BFP, 505–550 nm for
697 GFP, and 572–615 nm for mCherry. Chloroplast autofluorescence was labeled using excitation at 637
698 nm and emission in the range of 660–737 nm. For imaging of NRC4 haustoria accumulation, *P.*
699 *infestans* inoculation was performed as described below. After 1 day of inoculation, leaf discs from
700 the infected regions were imaged using a 40x water immersion objective lens on a Leica Stellaris 8
701 inverted confocal microscope as described before (Yuen *et al*, 2024a). The single-plane images were
702 exported to Fiji (ImageJ) software for quantitative analysis. GFP and RFP signals were measured at

703 selected areas (5 μm) spanning the peripheral cytoplasm and across the extrahaustorial membrane
704 (EHM).
705
706 **Inoculation of *Phytophthora infestans***
707 *P. infestans* 214009 (a gift from Dr. Jin-Hsing Huang, Taiwan Agriculture Research Institute) was
708 originally isolated from Taiping, Taichung City, Taiwan. *P. infestans* was maintained on Rye sucrose
709 medium at 19ºC under dark conditions. Before performing the focal accumulation assay for NRC4, *P.*
710 *infestans* was subcultured on detached *N. benthamiana* leaves. For the EHM focal accumulation assay,
711 leaves from 4-week-old *nrc2/3/4*_KO *N. benthamiana* plants were infiltrated with *Agrobacterium*
712 containing either wild-type or hydrophobic core mutant NRC4 constructs and a cytosolic RFP marker.
713 Zoospores were collected from sporangia on *P. infestans*-infected *N. benthamiana* leaves by
714 incubating the sporangia in sterile water at 4ºC as previously described (Yuen *et al*, 2024b). The
715 zoospores were then inoculated onto detached *N. benthamiana* leaves 2 days after transient expression
716 of NRC4 variants.
717
718 **Protein structure prediction**
719 To identify the position of the conserved hydrophobic residue candidates, we applied AlphaFold 3 to
720 predict the NRC4 monomer (pTM=0.82) (Abramson *et al*, 2024). Assuming similar protein
721 conformation, we superimposed the NRC4 monomer to the published NbNRC2 dimer (PDB: 8RFH)
722 by using the "Matchmaker" function to further correct the NbNRC4 structure we obtained from
723 AlphaFold3 (Abramson *et al*, 2024). Since the CC domain is missing in this NbNRC2 homodimer
724 structure and may make the CC domain differ from the current model, we cross-compared the
725 position of the hydrophobic core on the NbNRC4 resistosome structure (PDB: 9CC8).
726
727 **Phylogenetic analysis**
728 The amino acid sequences of the NB-ARC domain of the NRC superfamily from 20 species
729 representing various genera within the Solanaceae were extracted from the dataset in the NLRdome
730 (Sugihara *et al*, 2023). A total of 2,581 sequences, including reference NLR sequences, were aligned
731 using MAFFT (Katoh *et al*, 2019). Gaps in the aligned sequences were manually removed in MEGA
732 (Molecular Evolutionary Genetics Analysis), and the trimmed amino acid sequences were used for
733 phylogenetic analysis in IQtree (Kumar *et al*, 2016; Minh *et al*, 2020). The phylogenetic analysis
734 employed the Maximum Likelihood method with the JTT+F+R10 evolutionary model and 1000
735 bootstrap tests to assess the reliability of the tree. NLR clades were further categorized based on the
736 grouping criteria outlined in the previous study (Seong *et al*, 2020).
737
738 **Hydrophobic core amino acid logo creation and entropy analysis**

The full-length NLR amino acid sequences and the CC domain sequences from each clade were extracted and aligned using MAFFT, with NRC2/3/4 serving as the reference for identifying the hydrophobic core. To create the amino acid logo, the corresponding residues of the hydrophobic core in each clade were extracted, and the reference NRC2/3/4 sequences were removed. Amino acid logos for each clade were then generated based on the extracted hydrophobic core residues using WebLogo 3 (https://weblogo.threeplusone.com/create.cgi) (Crooks *et al*, 2004). After CC domain alignment and removal of NRC2/3/4 sequences, the remaining sequences were subjected to entropy analysis. Shannon entropy was calculated using an online tool developed by the Los Alamos National Laboratory (https://www.hiv.lanl.gov/content/sequence/ENTROPY/entropy.html). The hydrophobic core was labeled, and a cutoff score of 0.75 was applied to identify highly variable residues compared to the NRC group. Detailed analysis results are included in the Dataset S3.

Acknowledgments

We thank Mark Youles (SynBio, The Sainsbury Laboratory, UK) for sharing plasmids for molecular cloning. We thank Mei-Jane Fang and Ji-Ying Huang in the Live-Cell-Imaging Core Lab (Institute of Plant and Microbial Biology, Academia Sinica, Taiwan) and Shu-Chen Shen in the Advanced Optical Microscope Core Facility (Agricultural Biotechnology Research Center, Academia Sinica, Taiwan) for help with confocal imaging. We thank Dr. Jin-Hsing Huang (Taiwan Agriculture Research Institute) for providing the *P. infestans* isolate 214009 and advice on pathogen inoculation. This project was funded by the 2030 Emerging Young Scholar Program of the National Science and Technology Council (NSTC) of Taiwan (NSTC-112-2628-B-001-007), a bilateral exchange grant of NSTC and Royal Society (UK) (NSTC-113-2927-I-001-514, IEC\NSFC\233289), and the intramural fund of Institute of Plant and Microbial Biology, Academia Sinica, Taiwan. ELHY and TB are funded by Biotechnology and Biological Sciences Research Council (BBSRC) BB/X016382/1.

Author Contributions

HYW and CHW contributed to the conceptualization of the project. HYW contributed to data curation. HYW, ELHY, and CHW contributed to the formal analysis. HWY, ELHY, and CHW contributed to the investigation. KTL and FJG contributed to the methodology. TOB and CHW supervised the research and acquired funding. CHW managed the project. HYW and ELHY contributed to data visualization. HYW and CHW wrote the initial manuscript draft. HYW, ELHY, and CHW edited the manuscript.

Data Availability

All study data are included in the article and/or supporting information.

Competing Interest Statement

TOB receives funding from the industry on NLR biology, and is a co-founder of Resurrect Bio Ltd. The remaining authors have no conflicts of interest to declare.

813 **Supplementary Data**

814 Figure S1. Alignment of the CC domain of NbNRC2/3/4 and AtZAR1.

815 Figure S2. The protein accumulation of NRC4 hydrophobic residues mutant variants.

816 Figure S3. The localization of the hydrophobic core in the NRC4 dimer and the resistosome.

817 Figure S4. The hydrophobic core of the CC domain in the NRC2 dimer and the resistosome

818 Figure S5. $NRC4^{AAA}$ showed no cell death at 2 dpi compared to wild-type NRC4.

819 Figure S6. Mutations on the hydrophobic core do not affect NRC4 subcellular localization in the
820 resting state.

821 Figure S7. The mutation on A72 delays the formation of the resistosome and puncta on the plasma
822 membrane.

823 Figure S8. Mutations of hydrophobic residues outside the hydrophobic core did not affect the
824 association of the NRC4 CC domain with phospholipids.

825 Figure S9. Mutations of the hydrophobic core do not affect the NRC4 focal accumulation on the EHM.

826 Figure S10. Phylogenetic tree of the NRC superclade and selected singleton NLR groups (R2, Rpi-
827 vnt1, and ZAR1).

828 Figure S11. Quantitative cell death result of NRC2, NRC3, R2, and ZAR1 variants.

829 Figure S12. The EDVID motif is absent in R2.

830 Table S1. List of the constructs used in cell death assays.

831 Table S2. List of the constructs used in lipid binding assays.

832 Table S3. List of the constructs used in cell biology assays.

833 Table S4. List of the constructs used in BN-PAGE assays.

834 Table S5. List of the constructs used in cell fractionation assays.

835 Table S6. List of the constructs used in focal assays.

836 Dataset S1. List of primers used in this study. (XLSX)

837 Dataset S2. List of plasmids used in this study. (XLSX)

838 Dataset S3. Results of entropy analysis. (XLSX)

839 File S1. NRC superfamily phylogenetic tree files of 22 species.

840 File S2. ZAR1 group CC domain alignment. (TXT)

841 File S3. G5 group CC domain alignment. (TXT)

842 File S4. G11 group CC domain alignment. (TXT)

843 File S5. G8 group CC domain alignment. (TXT)

844 File S6. G12 group CC domain alignment. (TXT)

845 File S7. G2 group CC domain alignment. (TXT)

846 File S8. G9 group CC domain alignment. (TXT)

847 File S9. G14 group CC domain alignment. (TXT)

848

849

850 **References**

851

852 Abas L & Luschnig C (2010) Maximum yields of microsomal-type membranes from small amounts
853 of plant material without requiring ultracentrifugation. *Analytical Biochemistry* 401: 217–227

854 Abramson J, Adler J, Dunger J, Evans R, Green T, Pritzel A, Ronneberger O, Willmore L, Ballard AJ,
855 Bambrick J, *et al* (2024) Accurate structure prediction of biomolecular interactions with
856 AlphaFold 3. *Nature* 630: 493–500

857 Adachi H, Contreras MP, Harant A, Wu C, Derevnina L, Sakai T, Duggan C, Moratto E, Bozkurt TO,
858 Maqbool A, *et al* (2019a) An N-terminal motif in NLR immune receptors is functionally
859 conserved across distantly related plant species. *eLife* 8: e49956

860 Adachi H, Derevnina L & Kamoun S (2019b) NLR singletons, pairs, and networks: evolution,
861 assembly, and regulation of the intracellular immunoreceptor circuitry of plants. *Curr Opin*
862 *Plant Biol* 50: 121–131

863 Bi G, Su M, Li N, Liang Y, Dang S, Xu J, Hu M, Wang J, Zou M, Deng Y, *et al* (2021) The ZAR1
864 resistosome is a calcium-permeable channel triggering plant immune signaling. *Cell* 184:
865 3528-3541.e12

866 Bozkurt TO & Kamoun S (2020) The plant–pathogen haustorial interface at a glance. *Journal of Cell*
867 *Science* 133: jcs237958

868 Bozkurt TO, Schornack S, Win J, Shindo T, Ilyas M, Oliva R, Cano LM, Jones AME, Huitema E, van
869 der Hoorn RAL, *et al* (2011) Phytophthora infestans effector AVRblb2 prevents secretion of a
870 plant immune protease at the haustorial interface. *Proceedings of the National Academy of*
871 *Sciences* 108: 20832–20837

872 Contreras MP, Lüdke D, Pai H, Toghani A & Kamoun S (2023a) NLR receptors in plant immunity:
873 making sense of the alphabet soup. *EMBO reports* 24: e57495

874 Contreras MP, Pai H, Thompson R, Marchal C, Claeys J, Adachi H & Kamoun S (2024) The
875 nucleotide-binding domain of NRC-dependent disease resistance proteins is sufficient to
876 activate downstream helper NLR oligomerization and immune signaling. *New Phytologist*
877 243: 345–361

878 Contreras MP, Pai H, Tumtas Y, Duggan C, Yuen ELH, Cruces AV, Kourelis J, Ahn H, Lee K, Wu
879 C, *et al* (2023b) Sensor NLR immune proteins activate oligomerization of their NRC helpers
880 in response to plant pathogens. *The EMBO Journal* 42: e111519

881 Crooks GE, Hon G, Chandonia J-M & Brenner SE (2004) WebLogo: A Sequence Logo Generator.
882 *Genome Res* 14: 1188–1190

883 Duggan C, Moratto E, Savage Z, Hamilton E, Adachi H, Wu C-H, Leary AY, Tumtas Y, Rothery SM,
884 Maqbool A, *et al* (2021) Dynamic localization of a helper NLR at the plant–pathogen
885 interface underpins pathogen recognition. *Proc Natl Acad Sci USA* 118: e2104997118

886 Duxbury Z, Wu C & Ding P (2021) A Comparative Overview of the Intracellular Guardians of Plants
887 and Animals: NLRs in Innate Immunity and Beyond. *Annual Review of Plant Biology* 72:
888 155–184

889 Engler C, Youles M, Gruetzner R, Ehnert T-M, Werner S, Jones JDG, Patron NJ & Marillonnet S
890 (2014) A Golden Gate Modular Cloning Toolbox for Plants. *ACS Synth Biol* 3: 839–843

891 Förderer A, Li E, Lawson AW, Deng Y, Sun Y, Logemann E, Zhang X, Wen J, Han Z, Chang J, *et al*
892 (2022) A wheat resistosome defines common principles of immune receptor channels. *Nature*
893 610: 532–539

894 Foster SJ, Park T-H, Pel M, Brigneti G, Śliwka J, Jagger L, van der Vossen E & Jones JDG (2009)
895 Rpi-vnt1.1, a Tm-22 Homolog from Solanum venturii, Confers Resistance to Potato Late
896 Blight. *MPMI* 22: 589–600

897 Gilroy EM, Hein I, Van Der Hoorn R, Boevink PC, Venter E, McLellan H, Kaffarnik F, Hrubikova K,
898 Shaw J, Holeva M, *et al* (2007) Involvement of cathepsin B in the plant disease resistance
899 hypersensitive response. *The Plant Journal* 52: 1–13

900 Goh F-J, Huang C-Y, Derevnina L & Wu C-H (2024) NRC Immune receptor networks show
901 diversified hierarchical genetic architecture across plant lineages. *The Plant Cell* 36: 3399–
902 3418

903 Huang S, Jia A, Song W, Hessler G, Meng Y, Sun Y, Xu L, Laessle H, Jirschitzka J, Ma S, *et al*
904 (2022) Identification and receptor mechanism of TIR-catalyzed small molecules in plant
905 immunity. *Science* 377: eabq3297

906 Jacob P, Kim NH, Wu F, El-Kasmi F, Chi Y, Walton WG, Furzer OJ, Lietzan AD, Sunil S,
907 Kempthorn K, *et al* (2021) Plant "helper" immune receptors are Ca2+-permeable nonselective
908 cation channels. *Science* 373: 420–425

909 Jia A, Huang S, Song W, Wang J, Meng Y, Sun Y, Xu L, Laessle H, Jirschitzka J, Hou J, *et al* (2022)
910 TIR-catalyzed ADP-ribosylation reactions produce signaling molecules for plant immunity.
911 *Science* 377: eabq8180

912 Jones JDG & Dangl JL (2006) The plant immune system. *Nature* 444: 323–329

913 Jones JDG, Staskawicz BJ & Dangl JL (2024) The plant immune system: From discovery to
914 deployment. *Cell* 187: 2095–2116

915 Katoh K, Rozewicki J & Yamada KD (2019) MAFFT online service: multiple sequence alignment,
916 interactive sequence choice and visualization. *Briefings in Bioinformatics* 20: 1160–1166

917 King FJ, Yuen ELH & Bozkurt TO (2024) Border Control: Manipulation of the Host–Pathogen
918 Interface by Perihaustorial Oomycete Effectors. *MPMI* 37: 220–226

919 Kumar S, Stecher G & Tamura K (2016) MEGA7: Molecular Evolutionary Genetics Analysis
920 Version 7.0 for Bigger Datasets. *Molecular Biology and Evolution* 33: 1870–1874

921 Lin X, Olave-Achury A, Heal R, Pais M, Witek K, Ahn H-K, Zhao H, Bhanvadia S, Karki HS, Song
922 T, *et al* (2022) A potato late blight resistance gene protects against multiple *Phytophthora*
923 species by recognizing a broadly conserved RXLR-WY effector. *Molecular Plant* 15: 1457–
924 1469

925 Liu F, Yang Z, Wang C, You Z, Martin R, Qiao W, Huang J, Jacob P, Dangl JL, Carette JE, *et al*
926 (2024) Activation of the helper NRC4 immune receptor forms a hexameric resistosome. *Cell*
927 187: 4877-4889.e15

928 Ma S, An C, Lawson AW, Cao Y, Sun Y, Tan EYJ, Pan J, Jirschitzka J, Kümmel F, Mukhi N, *et al*
929 (2024) Oligomerization-mediated autoinhibition and cofactor binding of a plant NLR. *Nature*
930 632: 869–876

931 Ma S, Lapin D, Liu L, Sun Y, Song W, Zhang X, Logemann E, Yu D, Wang J, Jirschitzka J, *et al*
932 (2020) Direct pathogen-induced assembly of an NLR immune receptor complex to form a
933 holoenzyme. *Science* 370: eabe3069

934 Madhuprakash J, Toghani A, Contreras MP, Posbeyikian A, Richardson J, Kourelis J, Bozkurt TO,
935 Webster MW & Kamoun S (2024) A disease resistance protein triggers oligomerization of its
936 NLR helper into a hexameric resistosome to mediate innate immunity. *Science Advances* 10:
937 eadr2594

938 Martin R, Qi T, Zhang H, Liu F, King M, Toth C, Nogales E & Staskawicz BJ (2020) Structure of the
939 activated ROQ1 resistosome directly recognizing the pathogen effector XopQ. *Science* 370:
940 eabd9993

941 Minh BQ, Schmidt HA, Chernomor O, Schrempf D, Woodhams MD, von Haeseler A & Lanfear R
942 (2020) IQ-TREE 2: New Models and Efficient Methods for Phylogenetic Inference in the
943 Genomic Era. *Molecular Biology and Evolution* 37: 1530–1534

944 Ngou BPM, Ahn H-K, Ding P & Jones JDG (2021) Mutual potentiation of plant immunity by cell-
945 surface and intracellular receptors. *Nature* 592: 110–115

946 Rairdan GJ, Collier SM, Sacco MA, Baldwin TT, Boettrich T & Moffett P (2008) The Coiled-Coil
947 and Nucleotide Binding Domains of the Potato Rx Disease Resistance Protein Function in
948 Pathogen Recognition and Signaling. *The Plant Cell* 20: 739–751

949 Rausche J, Stenzel I, Stauder R, Fratini M, Trujillo M, Heilmann I & Rosahl S (2021) A
950 phosphoinositide 5-phosphatase from Solanum tuberosum is activated by PAMP-treatment
951 and may antagonize phosphatidylinositol 4,5-bisphosphate at Phytophthora infestans infection
952 sites. *New Phytologist* 229: 469–487

953 Saile SC, Ackermann FM, Sunil S, Keicher J, Bayless A, Bonardi V, Wan L, Doumane M, Stöbbe E,
954 Jaillais Y, *et al* (2021) Arabidopsis ADR1 helper NLR immune receptors localize and
955 function at the plasma membrane in a phospholipid dependent manner. *New Phytologist* 232:
956 2440–2456

957 Sakai T, Contreras MP, Martinez-Anaya C, Lüdke D, Kamoun S, Wu C-H & Adachi H (2024) The
958 NRC0 gene cluster of sensor and helper NLR immune receptors is functionally conserved
959 across asterid plants. *The Plant Cell* 36: 3344–3361

960 Selvaraj M, Toghani A, Pai H, Sugihara Y, Kourelis J, Yuen ELH, Ibrahim T, Zhao H, Xie R,
961 Maqbool A, *et al* (2024) Activation of plant immunity through conversion of a helper NLR
962 homodimer into a resistosome. *PLOS Biology* 22: e3002868

963 Seong K, Seo E, Witek K, Li M & Staskawicz B (2020) Evolution of NLR resistance genes with
964 noncanonical N-terminal domains in wild tomato species. *New Phytologist* 227: 1530–1543

965 Shepherd S, Yuen ELH, Carella P & Bozkurt TO (2023) The wheels of destruction: Plant NLR
966 immune receptors are mobile and structurally dynamic disease resistance proteins. *Current*
967 *Opinion in Plant Biology* 74: 102372

968 Sugihara Y, Toghani A, Kamoun S & Kourelis J (2023) NLRome dataset from 124 genomes of plants
969 in the Solanaceae family. doi:10.5281/zenodo.10354350 [DATASET]

970 Tai TH, Dahlbeck D, Clark ET, Gajiwala P, Pasion R, Whalen MC, Stall RE & Staskawicz BJ (1999)
971 Expression of the Bs2 pepper gene confers resistance to bacterial spot disease in tomato.
972 *Proceedings of the National Academy of Sciences* 96: 14153–14158

973 Wan L, Essuman K, Anderson RG, Sasaki Y, Monteiro F, Chung E-H, Osborne Nishimura E,
974 DiAntonio A, Milbrandt J, Dangl JL, *et al* (2019) TIR domains of plant immune receptors are
975 NAD+-cleaving enzymes that promote cell death. *Science* 365: 799–803

976 Wang J, Hu M, Wang J, Qi J, Han Z, Wang G, Qi Y, Wang H-W, Zhou J-M & Chai J (2019a)
977 Reconstitution and structure of a plant NLR resistosome conferring immunity. *Science* 364:
978 eaav5870

979 Wang S, Boevink PC, Welsh L, Zhang R, Whisson SC & Birch PRJ (2017) Delivery of cytoplasmic
980 and apoplastic effectors from Phytophthora infestans haustoria by distinct secretion pathways.
981 *New Phytologist* 216: 205–215

982 Wang S, McLellan H, Bukharova T, He Q, Murphy F, Shi J, Sun S, van Weymers P, Ren Y, Thilliez
983 G, *et al* (2019b) Phytophthora infestans RXLR effectors act in concert at diverse subcellular
984 locations to enhance host colonization. *Journal of Experimental Botany* 70: 343–356

985 Wang Z, Liu X, Yu J, Yin S, Cai W, Kim NH, El Kasmi F, Dangl JL & Wan L (2023) Plasma
986 membrane association and resistosome formation of plant helper immune receptors.
987 *Proceedings of the National Academy of Sciences* 120: e2222036120

988 Weber E, Engler C, Gruetzner R, Werner S & Marillonnet S (2011) A modular cloning system for
989 standardized assembly of multigene constructs. *PLoS One* 6: e16765

990 Win J, Kamoun S & Jones AME (2011) Purification of Effector–Target Protein Complexes via
991 Transient Expression in Nicotiana benthamiana. In *Plant Immunity: Methods and Protocols*,
992 McDowell JM (ed) pp 181–194. Totowa, NJ: Humana Press

993 Wróblewski T, Spiridon L, Martin EC, Petrescu A-J, Cavanaugh K, Truco MJ, Xu H, Gozdowski D,
994 Pawłowski K, Michelmore RW, *et al* (2018) Genome-wide functional analyses of plant
995 coiled–coil NLR-type pathogen receptors reveal essential roles of their N-terminal domain in
996 oligomerization, networking, and immunity. *PLOS Biology* 16: e2005821

997 Wu C-H, Abd-El-Haliem A, Bozkurt TO, Belhaj K, Terauchi R, Vossen JH & Kamoun S (2017) NLR
998 network mediates immunity to diverse plant pathogens. *Proceedings of the National Academy*
999 *of Sciences* 114: 8113–8118

1000 Wu C-H, Adachi H, De la Concepcion JC, Castells-Graells R, Nekrasov V & Kamoun S (2020)
1001 NRC4 Gene Cluster Is Not Essential for Bacterial Flagellin-Triggered Immunity1 [OPEN].
1002 *Plant Physiology* 182: 455–459

1003 Wu C-H, Derevnina L & Kamoun S (2018) Receptor networks underpin plant immunity. *Science* 360:
1004 1300–1301

1005 Yu H, Xu W, Chen S, Wu X, Rao W, Liu X, Xu X, Chen J, Nishimura MT, Zhang Y, *et al* (2024)
1006 Activation of a helper NLR by plant and bacterial TIR immune signaling. *Science* 386: 1413–
1007 1420

1008 Yuen ELH, Leary AY, Clavel M, Tumtas Y, Mohseni A, Zhao J, Picchianti L, Jamshidiha M, Pandey
1009 P, Duggan C, *et al* (2024a) A RabGAP negatively regulates plant autophagy and immune
1010 trafficking. *Current Biology* 34: 2049-2065.e6

1011 Yuen ELH, Shepherd S & Bozkurt TO (2023) Traffic Control: Subversion of Plant Membrane
1012 Trafficking by Pathogens. *Annu Rev Phytopathol* 61: 325–350

1013 Yuen ELH, Tumtas Y, King F, Ibrahim T, Chan LI, Evangelisti E, Tulin F, Skłenar J, Menke FLH,

1014 Kamoun S, *et al* (2024b) A pathogen effector co-opts a host RabGAP protein to remodel
1015 pathogen interface and subvert defense-related secretion. *Science Advances* 10: eado9516